



Cite this: *Nanoscale*, 2017, 9, 10044

Aggregation dynamics of nanoparticles at solid–liquid interfaces†

Xuezheng Tian,^{a,b} Haimei Zheng^{b,c,d} and Utkur Mirsaidov^{*,a,e,f,g}

The dynamics of molecules or nanoparticles (NPs) at solid–liquid interfaces plays an important role in many natural and industrial processes. However, the effects of a solid–liquid interface on NP motion and on the interactions between these NPs is still not well understood. Here, using *in situ* liquid cell transmission electron microscopy (TEM), we directly observed the movement of gold NPs and their aggregation dynamics at solid–liquid interfaces. We found that the solid surfaces transiently pin the NPs during their aggregation, dampening their translational and rotational movements. This surface pinning reduces both the movement of NPs and their aggregation rate as the aggregates grow by attachment. However, the pinning of the NP aggregates affects their translational and rotational motions differently. Initially, with increasing aggregate size, the aggregate's translational motion dampens more than its rotational motion. Consequently, the initial aggregation stages are driven by both the translational and rotational motions, whereas the rotational motion dominates the later aggregation stages. Our results provide insight into the movements of NPs and their aggregates at solid–liquid interfaces, which may assist in the future design and control of NP assemblies at interfaces.

Received 21st March 2017,
Accepted 3rd June 2017

DOI: 10.1039/c7nr01985h

rscl.li/nanoscale

Introduction

The dynamics of nanoparticles (NPs) at solid–liquid interfaces plays an important role in many chemical and biological phenomena, such as self-assembly,^{1,2} heterocatalysis^{3,4} and a variety of macromolecular processes occurring on biological cell membranes.^{5,6} In solution, the interactions between NPs and surfaces influences NP movements, and may affect their assembly and aggregation rates on surfaces.^{7–10} For example, the diffusive movements of NPs at solid–liquid interfaces are known to be 10^3 – 10^9 times slower than their bulk Brownian diffusion.^{10–15} Also, NPs at a solid–liquid interface may translocate through stick-slip motion due to strong interactions between the NPs and surfaces.^{16–18} Furthermore,

recent studies based on NPs with anisotropic shapes revealed that the adsorption of nanorods^{19,20} or nanocubes¹⁸ onto a solid surface at the solid–liquid interface might limit their movement only to intermittent rotations. The detailed physical models describing the role of particle–particle or particle–surface interactions at the nanoscale are still lacking.^{21,22} Consequently, the description of systems that accounts for the collective behavior of NPs at solid–liquid interfaces in processes such as aggregation is even less clear.^{23–25} Time-resolved direct imaging of interacting NPs at the solid–liquid interface can provide valuable insight regarding the effects of the surface on the collective NP dynamics.

Here, using *in situ* transmission electron microscopy (TEM),^{26–29} we directly observed the aggregation dynamics of gold NPs at the SiN_x–water interface driven by the surface diffusion of the NPs. Our observations show that the solid surfaces may transiently pin the moving NPs and their aggregates. Thus, their overall motions slow down. The reduced mobility of the NPs and their aggregates also reduces their aggregation rates compared to the aggregation rates of freely diffusing NPs. Specifically, we found that the translational and rotational diffusion coefficients of aggregates at the solid–liquid interface are $\sim 10^6$ – 10^7 and $\sim 10^4$ – 10^5 times less than those in bulk solutions, respectively. The translational and rotational movements scale differently with the size of the aggregates. Thus, the modes of motion that drive the aggregation depend on the size of aggregates; early and late stages of aggregation are

^aCentre for BioImaging Sciences, Department of Biological Sciences, National University of Singapore, 117557, Singapore

^bBerkeley Education Alliance for Research in Singapore, 138602, Singapore

^cMaterials Sciences Division, Lawrence Berkeley National Laboratory, Berkeley, CA 94720, USA

^dDepartment of Materials Science and Engineering, University of California, Berkeley, CA 94720, USA

^eDepartment of Physics, National University of Singapore, 117551, Singapore

^fNUSNNI-NanoCore, National University of Singapore, 117411, Singapore

^gCentre for Advanced 2D Materials, National University of Singapore, 117546, Singapore. E-mail: mirsaidov@nus.edu.sg

† Electronic supplementary information (ESI) available. See DOI: 10.1039/c7nr01985h

driven by translational and rotational diffusions, respectively. Once the aggregate reaches a critical size ($\sim 800 \text{ nm}^2$ in the projected view), it is fully immobilized on the surface due to surface pinning at multiple sites. The interaction of NPs and their aggregates with surfaces explains the difference in the aggregation kinetics between NPs at solid–liquid interfaces and freely diffusing NPs in a bulk solution.

Experimental

Liquid cell and sample preparation

A schematic of a liquid cell is shown in Fig. 1A. Each liquid cell is composed of two $\sim 2.6 \text{ mm} \times 2.6 \text{ mm}$ Si chips, and each chip had a 20-nm-thick silicon nitride (SiN_x) membrane window with the dimensions of $\sim 30 \mu\text{m} \times 200 \mu\text{m}$ in the center of the chip. These custom liquid cell chips were fabri-

cated from 200- μm -thick and 4-inch-diameter double-side-polished (100) silicon wafers with a $\sim 20\text{-nm}$ -thick SiN_x film grown by low-pressure chemical vapor deposition (LPCVD) on both sides of the wafer. First, using photolithography, we patterned the membrane windows and grooves for cleaving the chips from the wafer. Next, using deep reactive ion etching (DRIE), we removed the SiN_x from the patterned area, followed by KOH etching to remove the exposed bulk Si. After the KOH etch, the wafer was cleaned with a sequential rinse in acetone, isopropanol, and water. Then, gold NPs were formed on one of the two membranes of the liquid cell by thermal deposition of gold (nominal thickness of 1 nm) directly onto the membrane of the chip at a rate of 0.5 \AA s^{-1} under high vacuum. The deposited gold naturally formed NPs with an average size of $\sim 11 \text{ nm}$ on the surface.³⁰ The average density of gold NPs on the SiN_x membrane was $\sim 1800 \text{ NP per } \mu\text{m}^2$, with a total surface coverage of $\sim 23\%$.

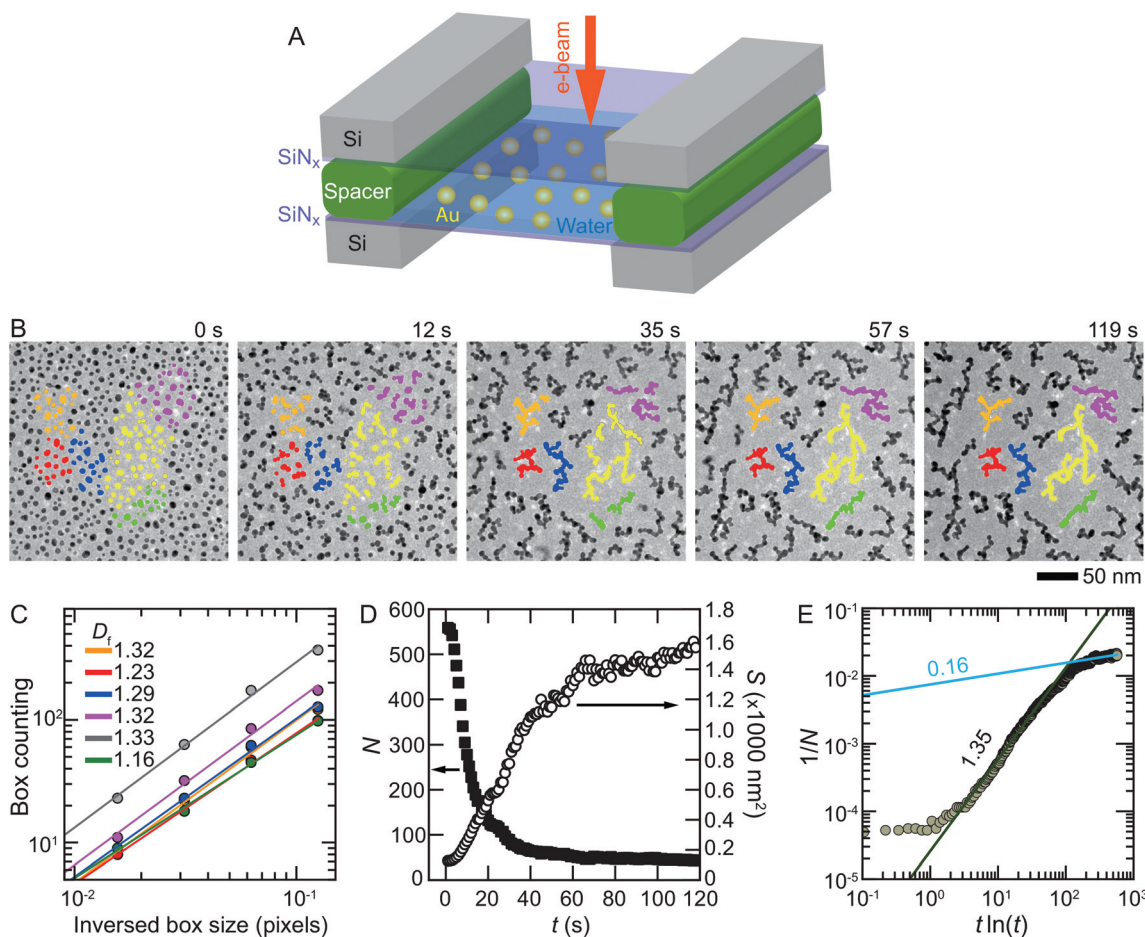


Fig. 1 Dynamics of nanoparticle (NP) aggregation on the SiN_x surface at a solid–liquid interface. (A) Experimental setup showing the gold NPs physisorbed onto the SiN_x membranes of a liquid cell. (B) *In situ* TEM time series images of the NP aggregation (ESI Movie S1†). The time evolution of the six aggregates is shown in different colors to highlight their aggregation dynamics. As the size of these aggregates increased, their growth and movement ceased ($t = 57 \text{ s}–119 \text{ s}$) owing to their pinning by the surface at multiple points. (C) The fractal dimensions (D_f) of six aggregates shown in (B), which were extracted using the box-counting method. (D) The number of aggregates in the field of view (N) and the average aggregate size (S), defined as a projected area of an aggregate, versus time (t). (E) The log–log plot of the inverse of the aggregate number ($1/N$) versus $t \ln t$, where the slope of the curve indicates the aggregation kinetics (z) (ESI section 3†). The slopes for the initial (green line) and later (blue line) aggregation stages are 1.35 and 0.16, respectively.

TEM imaging and image processing

After assembling the top and bottom chips into a liquid cell in the TEM flow holder (Hummingbird Scientific, Lacey, WA, USA), deionized water was loaded into the liquid cell using a syringe pump station. We then inserted the flow holder into a JEOL 2010F TEM operating at an acceleration voltage of 200 kV. The electron flux used for the *in situ* imaging experiments ranged from $\sim 10 \text{ e}^- (\text{\AA}^2 \text{ s})^{-1}$ to $\sim 120 \text{ e}^- (\text{\AA}^2 \text{ s})^{-1}$. Under the electron beam irradiation, the bulk water between the two membranes receded from the viewing area, leaving a thin water film on the SiN_x membrane surface^{14,31} where we observed the aggregation dynamics of the NPs. We recorded the movies using an Orius SC200 CCD camera (Gatan, Inc., Pleasanton, CA, USA) at a rate of 10 frames per second. We analyzed the dynamics of the NPs and their aggregates using our image processing algorithms implemented in the Miniconda Python software package³² (ESI section 1†).

Results and discussion

The gold NPs deposited on a SiN_x membrane were initially physisorbed onto the membrane due to the van der Waals (vdW) attraction between the NPs and the surface (Fig. 1B). When the NPs were exposed to an electron beam, they began to move within ~ 1 s. The detachment of the NPs from the surface, which results in their subsequent movement at the solid–liquid interface, is due to the electrostatic repulsion between the positively charged surface and the gold NPs.³³ Charging of the SiN_x membrane window and the gold NPs was induced by the electron beam irradiation.^{7,18}

To compare the collective aggregation kinetics of the NPs on the surface against the general aggregation kinetics of particles undergoing free, two-dimensional (2D) diffusion, we tracked the NP trajectories on the SiN_x surface. Fig. 1B shows the aggregation dynamics at the solid–liquid interface, which reveals that only nearby NPs collide and attach to form aggregates, and aggregation halts when the aggregates become large. In the context of aggregation kinetics, the fractal dimension, D_f , represents a measure of aggregate's packing density, *i.e.*, a small D_f corresponds to loose packing (ESI section 2†).³⁴ The fractal dimensions of these surface aggregates are in the range of 1.16 to 1.33 (Fig. 1C). These fractal dimensions are smaller than those of the aggregates that are formed by the 2D diffusion limited (1.44 ± 0.04) or the reaction (1.55 ± 0.03) limited aggregation process.^{24,35} This observation indicates that the aggregates forming at the solid–liquid interface by a surface diffusion are loosely packed. The small fractal dimension is consistent with the dampened diffusion of the surface aggregates, which we will discuss later. Moreover, in the case of free, 2D diffusion, the aggregate size (S), which is defined as the projected area of the aggregate, is expected to change linearly with time ($S(t) \sim t$), whereas the number of aggregates (N) is expected to be inversely proportional to time ($N(t) \sim t^{-1}$).^{8,24,36} This scaling for the aggregate size and number is different from our observations where the initial aggregation stage

was fast (*i.e.* the aggregate size increased rapidly as the number of aggregates decreased: $S(t) \sim t^x$ and $N(t) \sim t^{-x}$, $x \sim 2.42$), and later, the aggregation slowed down and came to a complete stop (Fig. 1D and ESI Movie S1†) (also see ESI Fig. S2† for more examples).

A more concise parameter to describe the aggregation rate is the aggregation kinetic exponent (z), which is defined as the slope of $1/N$ versus $t \ln t$ in a log–log plot:

$$z \sim \ln(1/N)/\ln[t \ln(t)] \quad (1)$$

Here, z is always positive and increases with the aggregation rate (ESI section 3†).²⁴ For the aggregation shown in Fig. 1B, the kinetic exponent starts as $z \approx 0$ ($t < 1$ s), reaches $z \approx 1.35$ ($t = 1$ s–30 s), and later ($t > 30$ s) decreases gradually towards $z \approx 0$ (Fig. 1E). These changes in the aggregation kinetic exponent correspond to the absence of NP movement prior to the electron beam induced membrane charging ($t < 1$ s), the fast aggregation of small NPs ($t = 1$ s–30 s), and the slow NP aggregation ($t > 30$ s) as the aggregates grow in size until the aggregation comes to a complete stop when the aggregates are immobilized on the surface. During the fast aggregation stage, the aggregation kinetic exponent ($z \approx 1.35$ at $t = 1$ s–30 s) is larger than the kinetic exponents for freely diffusing 2D ($z_{2D} = 0.75$) and 3D ($z_{3D} = 1.0$) aggregates.²⁴ This large value of the aggregation kinetic exponent during $t = 1$ s–30 s is consistent with a high NP density at the beginning ($\sim 23\%$ NP coverage on the SiN_x surface), which increases the initial probability of collisions between the NPs.³⁶

To understand the difference between the aggregation dynamics of the surface NPs observed here and NPs undergoing free, 2D diffusion, we looked at the movement of individual aggregates within the different aggregation stages, as shown in Fig. 2. Here, all the NPs were confined to the SiN_x –water interface in a thin water layer ($\lesssim 20$ nm) and therefore, only 2D fractals were formed *via* the collision and attachment of the NPs and their aggregates. Furthermore, we found that most of the aggregates were pinned to the surface to some extent. The pinning of the NPs and their aggregates causes a substantial reduction in their translational movements, and their translocation takes place by hopping between different pinning sites. When the NPs and aggregates are pinned to the surface at a single pinning site, they can undergo in-plane rotation (Fig. 2).

The pinning of the aggregates depends on their size, which in turn affects their growth kinetics. In the early stages of aggregation, most of the NPs and small aggregates can easily de-pin from the surface. We found only a few strongly pinned NPs that remained fixed on the surface, as shown in Fig. 2A. As the size of the NP aggregates increases, they are more likely to adsorb to the surface, which reduces their translational motion. In this stage, in addition to the translational diffusion, the contribution of the aggregates' rotational movement to their growth becomes significant. A single pinning site that traps an aggregate can serve as a pivot point for this aggregate to rotate, aiding its collision with and attachment to other NPs and aggregates (Fig. 2B). As the aggregates continue to grow, they can only

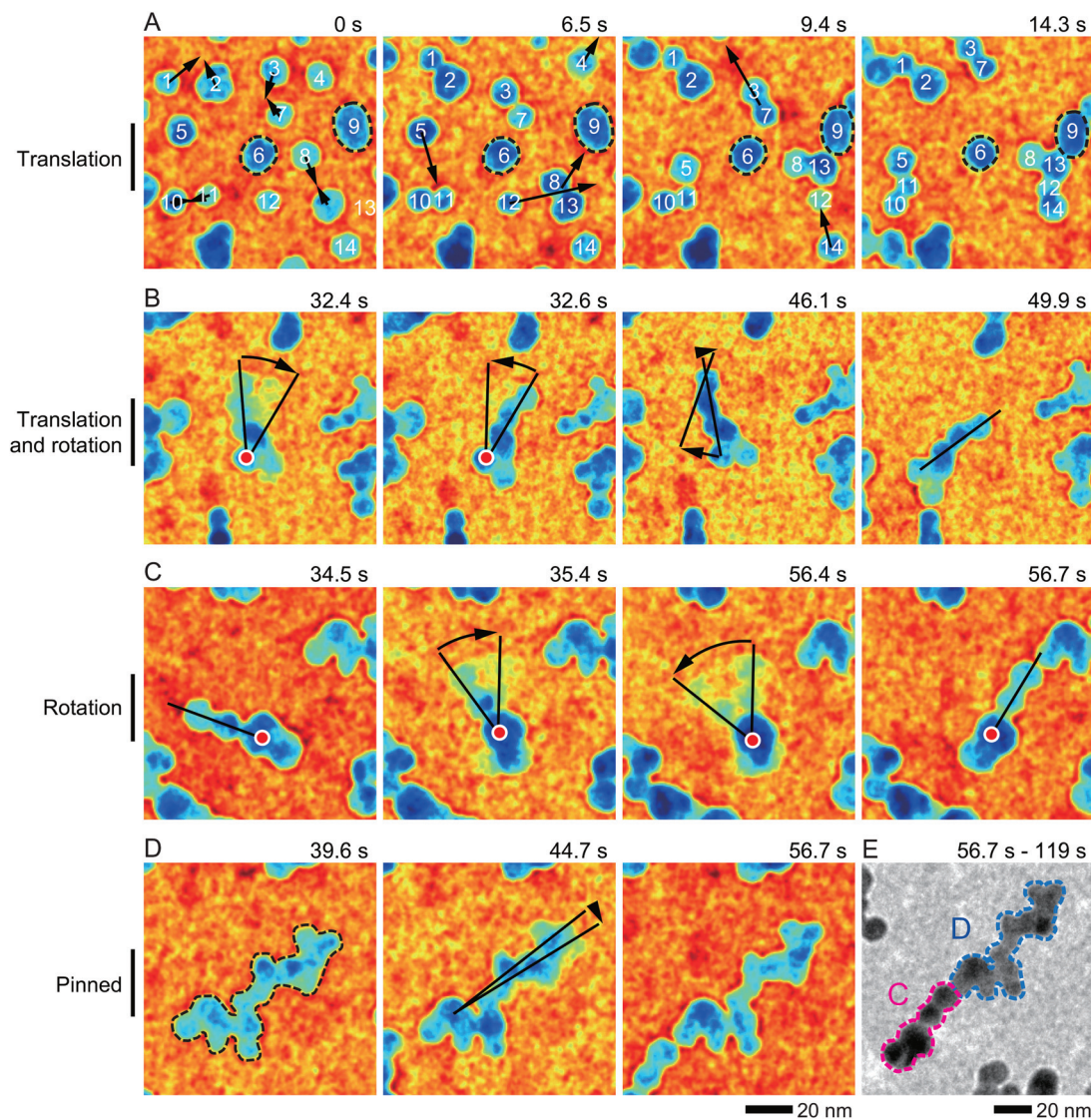


Fig. 2 *In situ* TEM time series images of the aggregation process. (A) The initial stage of aggregation occurs by the attachment of individual NPs and is driven by their translational movement. Most of the NPs are mobile, and very few NPs permanently adsorb to the surface (*i.e.*, only NP-6 and NP-9). (B, C) Once small aggregates are formed by NP attachment, their translational movement starts to slow down because they start to become pinned on the surface. At this point, the contribution of the aggregate's rotational movement to the aggregation process becomes more and more prominent. (D) Finally, when the aggregates are large, they are fully pinned to the surface, and they move very little. (E) An immobile aggregate that is formed by the attachment of the two aggregate fragments shown in (C) and (D). The arrows indicate the directions of the NP and aggregate movements. NPs circled by black dotted lines are permanently pinned to the surface. The red dots indicate the pinning sites, and the black lines on the aggregates show their rotation.

coalesce and grow through spurious rotations because, at this point, the surface pinning prevents any translational movement (Fig. 2C). Finally, when an aggregate is larger than ~ 800 nm², both the rotational and translational movements cease, and aggregation stops owing to the surface pinning of aggregates at multiple sites (Fig. 2D and E).

To understand the effects of the translational and rotational motions on different aggregation stages, we quantified the isolated translational and rotational motions of the pinned aggregates, as shown in Fig. 3. During the translational motion, the aggregate fluctuates around a pinning site, as it attempts to de-pin before hopping to a new location where it is

pinned again (Fig. 3A and B, and, ESI Movie S2[†]). In the case of rotational motion, the aggregate does not rotate freely around the pinning site, but swings back and forth within a certain angle ($-30^\circ \leq \theta_r \leq 30^\circ$) (Fig. 3D and E, and ESI Movie S3[†]). The histogram shown in Fig. 3E reveals two locations that transiently pin the rotating aggregate in addition to a single, strong pinning site around which the aggregate pivots. Therefore, intermittent rotations occur when aggregates are pinned at a single site, and these rotations cease during the simultaneous pinning of aggregates at more than one pinning site. Intermittent translation of aggregates occurs only in the absence of pinning.

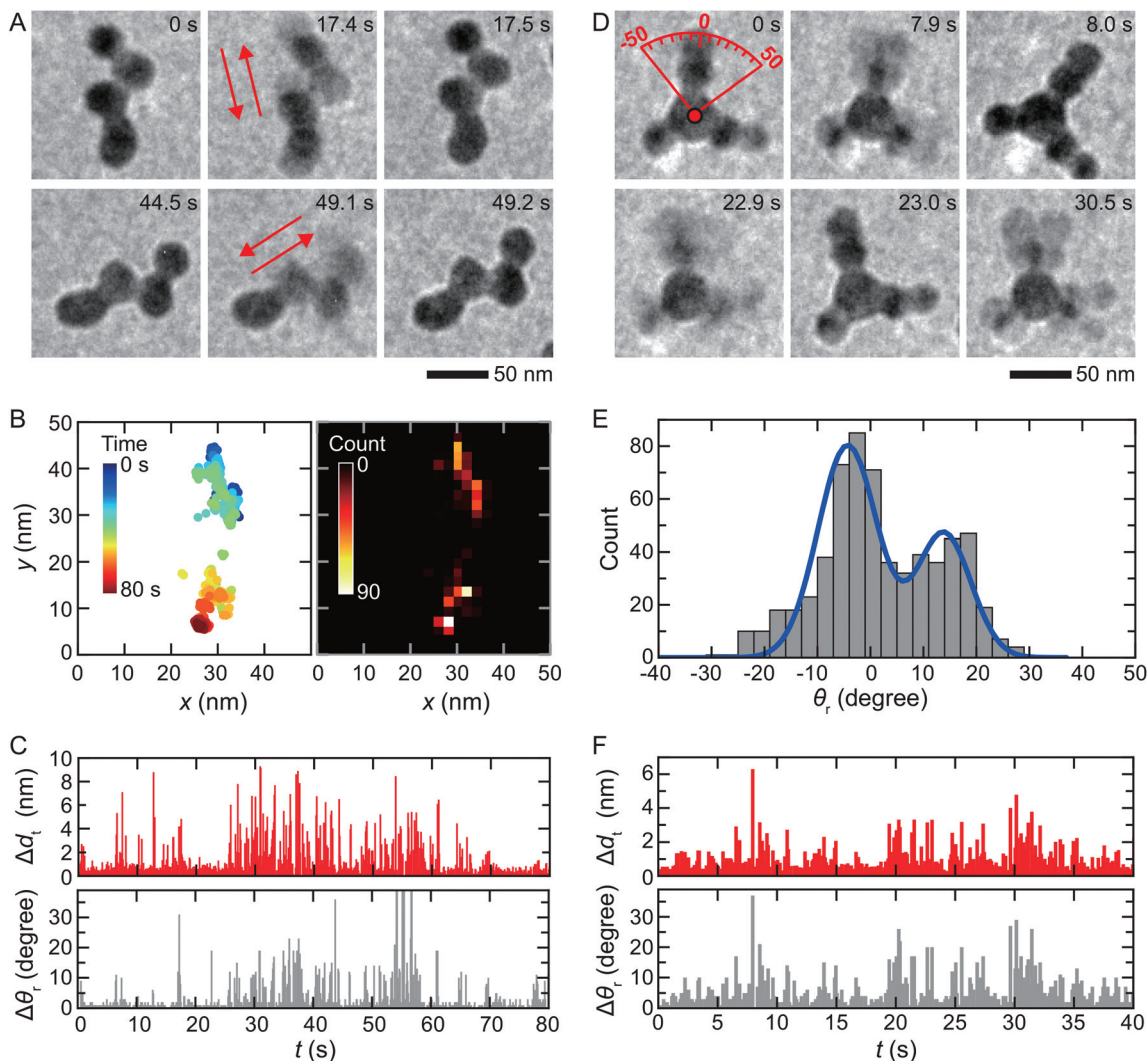


Fig. 3 Rotational and translational movements of the pinned aggregates. (A) *In situ* TEM time series images showing the fluctuation of a pinned aggregate during its translocation between two pinning sites. Top ($t = 0$ s–17.5 s) and bottom ($t = 44.5$ s–49.2 s) panels show the aggregate at its first and second pinning sites, respectively. The red arrows indicate the direction of the aggregate fluctuation at each pinning site. (B) (Left) Trajectory and (right) distribution of the same aggregate's centre of mass. (C) The translational (Δd_t) and rotational ($\Delta \theta_r$) displacements between two consecutive image frames (separated by $\Delta t = 0.1$ s) for the aggregate shown in (A). (D) *In situ* TEM time series images showing the rotation of a pinned aggregate. The scale bar for the rotation angle (red) indicates the range of the aggregate's rotation. The red dot indicates the location of the pinning site. (E) Distribution of the angular position of the aggregate during its 40 s rotation. (F) The translational and rotational displacements between two consecutive image frames (separated by $\Delta t = 0.1$ s) for the aggregate shown in (D).

The strength of surface pinning can be estimated from the aggregates' intermittent translational and rotational movements using the Arrhenius equation:³⁷

$$E_{\text{diff}} = -\ln(\Gamma/\nu) \cdot k_B T \quad (2)$$

where Γ is the successful translational and rotational jump frequency, ν is the jump-attempt frequency, T is the temperature, and k_B is the Boltzmann constant. From the probability distributions shown in Fig. 3B and E, we estimated the strength of the pinning interactions for the translational and rotational movements to be $\sim 19 k_B T$ and $\sim 20 k_B T$, respectively (ESI section 7†). The energy barrier associated with pinning is large

enough to transiently trap aggregates undergoing surface diffusion, and it is also comparable to the interaction strength of the physisorbed atoms undergoing surface diffusion.³⁸ The vdW attraction between the NPs and the membrane surface has the most significant contribution to the NP and aggregate pinning. In addition, SiN_x in water is known to hydrolyse into different surface charge groups, such as silanols (Si-OH) and silazanes ($\text{Si}_2\text{-NH}$, Si-NH_2),³⁹ which may alter the local electrostatic force and contribute to the pinning of the aggregates (see ESI section 8 for more discussion†).

The size-dependent movement of the aggregates results in a sequence of aggregation stages, which is also reflected in their translational (D_t) and rotational (D_r) diffusion coefficients. Our

analysis revealed that the D_t and D_r values for the NPs at the solid–liquid interface are about 10^6 – 10^7 and 10^4 – 10^5 times smaller than those of bulk diffusion, which is consistent with earlier reports of reduced NP mobility at solid–liquid interfaces.^{7,10,12–15,18} However, we found that during aggregation, D_t and D_r scale differently with the aggregate size (Fig. 4). The diffusion coefficients for translational and rotational movements scale as a power law: $D_t \sim S^{-1.41}$ for aggregate sizes $S < 3000 \text{ nm}^2$, $D_r \sim S^{-1.22}$ for aggregate sizes $S < 800 \text{ nm}^2$, and $D_r \sim S^{-4.99}$ for $800 \text{ nm}^2 < S < 3000 \text{ nm}^2$. Initially, the translational diffusion coefficient decreases faster than the rotational diffusion coefficient as the aggregate size increases. This change in the diffusion coefficient is consistent with the observed shift from translation-driven to rotation-driven aggregation during the aggregate growth. A further increase in the aggregate size ($S > 800 \text{ nm}^2$, which roughly corresponds to an aggregate of more than ~ 7 NPs) increases the likelihood of pinning by multiple sites on the surface simultaneously. The average rotational diffusion coefficient of an aggregate pinned at several sites decreases drastically (Fig. 4B), and the aggregation process stops.

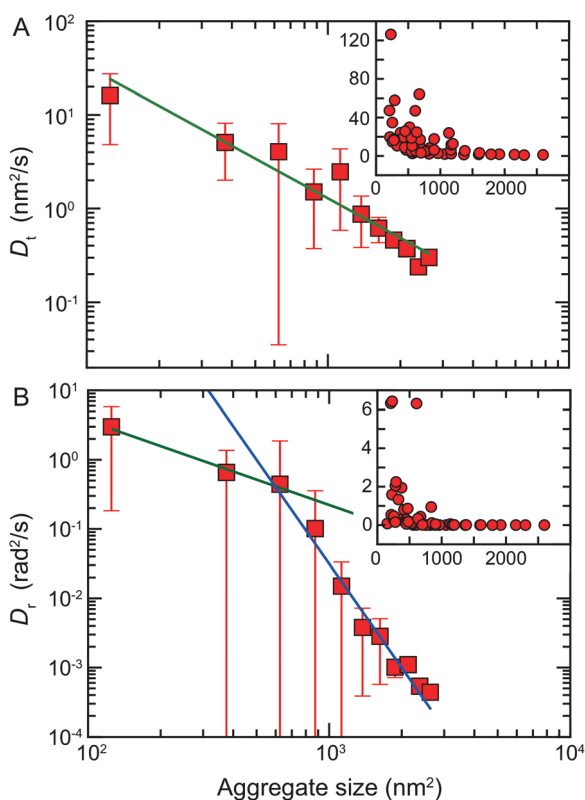


Fig. 4 Translational and rotational diffusions of NP aggregates. (A) Log–log plot of the average translational diffusion coefficient versus the aggregate size. The slope of the fit line is -1.41 . (B) Log–log plot of the average rotational diffusion coefficient versus the aggregate size. The slope of the fit is -1.22 and -4.99 for the green and blue lines, respectively. Error bars correspond to one standard deviation. Insets for (A) and (B) show the diffusion coefficients of individual aggregates in linear coordinates.

The strong size-dependent pinning of the aggregates also results in the smaller fractal dimensions observed in our experiment ($D_f \sim 1.16$ – 1.33) in comparison with the 2D aggregation of freely diffusing particles ($D_f \sim 1.44$).^{24,35} A small fractal dimension indicates loose aggregate packing, which is consistent with their reduced translational movement. The increase in the mobility of the aggregates on the surface due to the fluid flow drastically increases their fractal dimensions (ESI section 5 and Movie S4† show aggregates with a fractal dimension of $D_f = 1.63$ as a result of fluid-flow-induced aggregation).

Conclusions

In summary, we have shown that the size-dependent pinning of NP aggregates gives rise to four sequential aggregation stages at the SiN_x –water interface (Fig. 5): (1) The initial attachment between the NPs by the translational diffusion results in the formation of small aggregate fragments. (2) Intermediate size aggregates are formed by the attachment of these small aggregate fragments both through translation and rotation and these larger aggregates are more likely to pin on the surface owing to their increasing size. (3) The attachment between the pinned intermediate size aggregates occurs mostly through their rotational movement to form larger aggregates. (4) Finally, the aggregation process stops as pinning at multiple sites prevents any further movement of large aggregates. Our results provide a link between nanoscale movement and aggregation of NPs and are important for understanding processes such as NP self-assembly at interfaces.

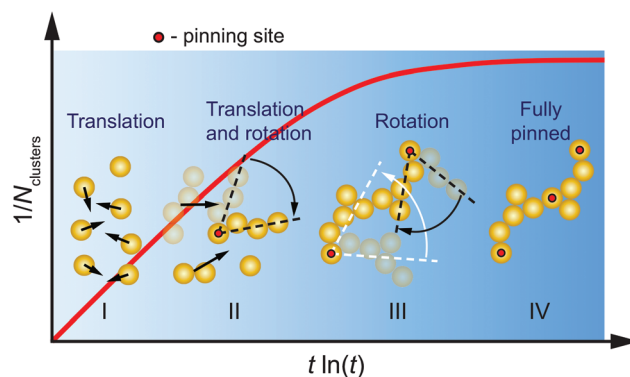


Fig. 5 Mechanism for NP aggregation at the solid–liquid interface. Schematic illustration displaying the three stages of NP aggregation at the solid–liquid interface. First, small aggregate fragments are formed via the translational motion of NPs that leads to their attachment. As the aggregation proceeds, the translational motion is suppressed because the large aggregate fragments are more prone to pinning by the surface. The rotational movement of these weakly pinned aggregates aids their further attachment and growth, and the aggregation dynamics gradually shifts from translation-driven to rotation-driven aggregation. Finally, when the aggregates are large enough their rotational motion also ceases because they are pinned to the surface at multiple pinning sites, which brings the aggregation process to a halt.

Acknowledgements

This work was supported by the Singapore Ministry of Education Academic Research Fund Tier 2 (MOE2015-T2-1-007). We thank U. Anand N. D. Loh and S. W. Chee for helpful discussion. H. Z. thanks the support from the U.S. Department of Energy Basic Energy Sciences Program Materials Sciences and Engineering Division under contract no. KC22ZH.

References

- 1 Y. Yin, Y. Lu, B. Gates and Y. Xia, *J. Am. Chem. Soc.*, 2001, **123**, 8718–8729.
- 2 Z. Nie, A. Petukhova and E. Kumacheva, *Nat. Nanotechnol.*, 2010, **5**, 15–25.
- 3 Y. Tachibana, L. Vayssieres and J. R. Durrant, *Nat. Photonics*, 2012, **6**, 511–518.
- 4 Y. Jiao, Y. Zheng, M. Jaroniec and S. Z. Qiao, *Chem. Soc. Rev.*, 2015, **44**, 2060–2086.
- 5 A. Kusumi and K. Suzuki, *Biochim. Biophys. Acta*, 2005, **1746**, 234–251.
- 6 J. Sankaran, M. Manna, L. Guo, R. Kraut and T. Wohland, *Biophys. J.*, 2009, **97**, 2630–2639.
- 7 E. R. White, M. Mecklenburg, B. Shevitski, S. B. Singer and B. C. Regan, *Langmuir*, 2012, **28**, 3695–3698.
- 8 J. M. Grogan, L. Rotkina and H. H. Bau, *Phys. Rev. E*, 2011, **83**, 061405.
- 9 Y. Liu, X.-M. Lin, Y. Sun and T. Rajh, *J. Am. Chem. Soc.*, 2013, **135**, 3764–3767.
- 10 T. J. Woehl and T. Prozorov, *J. Phys. Chem. C*, 2015, **119**, 21261–21269.
- 11 Q. Chen, H. Cho, K. Manthiram, M. Yoshida, X. Ye and A. P. Alivisatos, *ACS Cent. Sci.*, 2015, **1**, 33–39.
- 12 A. Verch, M. Pfaff and N. de Jonge, *Langmuir*, 2015, **31**, 6956–6964.
- 13 H. Zheng, S. A. Claridge, A. M. Minor, A. P. Alivisatos and U. Dahmen, *Nano Lett.*, 2009, **9**, 2460–2465.
- 14 J. Lu, Z. Aabdin, N. D. Loh, D. Bhattacharya and U. Mirsaidov, *Nano Lett.*, 2014, **14**, 2111–2115.
- 15 E. A. Ring and N. de Jonge, *Micron*, 2012, **43**, 1078–1084.
- 16 J. Zhao and S. Granick, *J. Am. Chem. Soc.*, 2004, **126**, 6242–6243.
- 17 M. J. Skaug, J. Mabry and D. K. Schwartz, *Phys. Rev. Lett.*, 2013, **110**, 256101.
- 18 S. W. Chee, Z. Baraissov, N. D. Loh, P. T. Matsudaira and U. Mirsaidov, *J. Phys. Chem. C*, 2016, **120**, 20462–20470.
- 19 Y. Gu, W. Sun, G. Wang and N. Fang, *J. Am. Chem. Soc.*, 2011, **133**, 5720–5723.
- 20 D. Xu, Y. He and E. S. Yeung, *Angew. Chem., Int. Ed. Engl.*, 2014, **53**, 6951–6955.
- 21 E. M. Hotze, T. Phenrat and G. V. Lowry, *J. Environ. Qual.*, 2010, **39**, 1909–1924.
- 22 C. A. S. Batista, R. G. Larson and N. A. Kotov, *Science*, 2015, **350**, 1242477.
- 23 M. Rahimi, T. F. Roberts, J. C. Armas-Pérez, X. Wang, E. Bukusoglu, N. L. Abbott and J. J. de Pablo, *Proc. Natl. Acad. Sci. U. S. A.*, 2015, **112**, 5297–5302.
- 24 P. Meakin, *Phys. Scr.*, 1992, **46**, 295.
- 25 K. J. M. Bishop, C. E. Wilmer, S. Soh and B. A. Grzybowski, *Small*, 2009, **5**, 1600–1630.
- 26 H. Zheng, R. K. Smith, Y.-W. Jun, C. Kisielowski, U. Dahmen and A. P. Alivisatos, *Science*, 2009, **324**, 1309–1312.
- 27 F. M. Ross, *Science*, 2015, **350**, aaa9886.
- 28 M. J. Williamson, R. M. Tromp, P. M. Vereecken, R. Hull and F. M. Ross, *Nat. Mater.*, 2003, **2**, 532–536.
- 29 N. D. Jonge, D. B. Peckys, G. J. Kremers and D. W. Piston, *Proc. Natl. Acad. Sci. U. S. A.*, 2009, **106**, 2159–2164.
- 30 C. Binns, *Surf. Sci. Rep.*, 2001, **44**, 1–49.
- 31 U. M. Mirsaidov, H. Zheng, D. Bhattacharya, Y. Casana and P. Matsudaira, *Proc. Natl. Acad. Sci. U. S. A.*, 2012, **109**, 7187–7190.
- 32 K. J. Millman and M. Aivazis, *Comput. Sci. Eng.*, 2011, **13**, 9–12.
- 33 J. N. Israelachvili, in *Intermolecular and Surface Forces*, 3rd edn, Academic Press, San Diego, 2011, pp. 291–340.
- 34 N. Sarkar and B. B. Chaudhuri, *IEEE Trans. Syst. Man Cybernet.*, 1994, **24**, 115–120.
- 35 M. Y. Lin, H. M. Lindsay, D. A. Weitz, R. C. Ball, R. Klein and P. Meakin, *Nature*, 1989, **339**, 360–362.
- 36 D. Fry, T. Sintes, A. Chakrabarti and C. M. Sorensen, *Phys. Rev. Lett.*, 2002, **89**, 148301.
- 37 K. J. Laidler, *J. Chem. Educ.*, 1984, **61**, 494.
- 38 M. C. Tringides, *Surface Diffusion: Atomistic and Collective Processes*, Springer, US, 2013.
- 39 J. Sonnefeld, *Colloids Surf., A*, 1996, **108**, 27–31.